Synthesis, Crystal and Electronic Structures and Thermoelectric Properties of the Novel Cluster Compound Ag3In2Mo15Se19

Patrick Gougeon, Philippe Gall, Rabih Al Rahal Al Orabi, Bruno Fontaine, Régis Gautier, Michel Potel, Tong Zhou, Bertrand Lenoir, Malika Colin, Christophe Candolfi, et al.

Synthesis, Crystal and Electronic Structures and Thermoelectric Properties of the Novel Cluster Compound $Ag_3In_2Mo_{15}Se_{19}$

Patrick Gougeon[1*], Philippe Gall[1], Rabih Al Rahal Al Orabi[1], Bruno Fontaine[1], Régis Gautier[1], Michel Potel[1], Tong Zhou[2], Bertrand Lenoir[2*], Malika Colin,[2] Christophe Candolfi,[2] Anne Dauscher[2].

[1]Sciences Chimiques de Rennes, UMR 6226 CNRS - Ecole Nationale Supérieure de Chimie de Rennes – I.N.S.A. - Université de Rennes1, Avenue de Général Leclerc, 35042 Rennes, France.

[2]Institut Jean Lamour, UMR 7198 CNRS-Nancy Université-UPVM, Ecole Nationale Supérieure des Mines de Nancy, Parc de Saurupt, 54042 Nancy, France.

KEYWORDS: cluster compound, single crystal X-ray diffraction, electronic structure, thermoelectric properties

Supporting Information Placeholder

ABSTRACT: Polycrystalline samples and single crystals of the new compound $Ag_3In_2Mo_{15}Se_{19}$ were synthesized by solid-state reaction in sealed molybdenum crucible at 1300°C. Its crystal structure (space group R-3c, a = 9.9755(1) Å, c = 57.2943(9) Å and Z = 6) was determined from single crystal X-ray diffraction data and constitutes an Ag-filled variant of the $In_2Mo_{15}Se_{19}$ structure-type containing octahedral Mo_6 and bioctahedral Mo_9 clusters in the ratio 1:1. The increase of the cationic charge transfer due to the silver insertion induces a modification of the Mo-Mo distances within the Mo clusters that is discussed with regard to the electronic structure. Transport properties were measured in a broad temperature range (2 – 1000 K) to assess the thermoelectric potential of this compound. The transport data indicate an electrical conduction dominated by electrons below 25K and by holes above this temperature. The metallic character of the transport properties in this material is in agreement with electronic band structure calculations carried out using the LMTO method. The complex unit cell together with the cage-like structure of this material results in very low thermal conductivity values (0.9 $W.m^{-1}.K^{-1}$ at 300 K) leading to a maximum estimated thermoelectric figure of merit ZT of 0.45 at 1100 K.

INTRODUCTION

Reduced molybdenum chalcogenides containing high nuclearity Mo clusters exhibit generally complex crystal structure with large voids totally or partially filled up by heavy atoms, which show high atomic displacement parameters.[1] This cage-like crystal structure makes Mo-cluster compounds prospective candidates for thermoelectric applications according to the PGEC (Phonon Glass Electron Crystal) concept introduced by Slack.[2] Such feature helps to reduce the lattice thermal conductivity, which stands for one of the prerequisite to achieve high thermoelectric efficiency. This is quantitatively captured through the dimensionless thermoelectric figure of merit defined as $ZT = \alpha^2 T / \rho(\kappa_e + \kappa_L)$ where α is the thermopower, ρ the electrical resistivity, κ_e and κ_L the electronic and lattice thermal conductivities, respectively, and T the absolute temperature.[3]

One of the most well-known families of chalcogenide is the Chevrel phase of general formula $M_xMo_6X_8$ (M can be alkaline, alkaline-earth, rare-earth, actinide or transition metal elements and X is usually a chalcogen i.e. S, Se or Te).[4,5] The crystal structure of this phase is composed of Mo_6X_8 building blocks, which consist of a Mo_6 octahedron, surrounded by eight chalcogens arranged in a distorted cube. The rhombohedral structure is then built by stacking the Mo_6X_8 units resulting in channels where additional atoms M can be inserted. These phases focused considerable attention not only due to their peculiar superconducting properties but also for their interesting thermoelectric properties.[6,7] Both metallic and semiconducting properties can be achieved depending on the nature and on the concentration of the filling atoms M. In particular, a maximum ZT value of 0.6 at 1150 K was obtained in double-filled $Cu/FeMo_6Se_8$ compounds.[7]

The nuclearity of the Mo clusters is however not limited to six and higher values can be achieved. The increase of the nuclearity results from the one-dimensional trans-face sharing of Mo_6 octahedra. The bioctahedral Mo_9 cluster stands for one building block composing the crystal structure of a large number of compounds. Specifically, this cluster was first observed alone in $Ag_xMo_9Se_{11}$ ($3.4 \le x \le 3.9$).[8,9] The crystal structure of these compounds is formed by the $Mo_9Se_{11}Se_6$ cluster unit, which can accommodate Ag atoms distributed over four independent sites. Recently, the high-temperature thermoelectric properties of $Ag_xMo_9Se_{11}$ ($3.4 \le x \le 3.9$) were reported.[10,11] Our study has revealed that the electronic properties can be tuned by varying the Ag content. The transport properties progressively evolve with increasing x from metallic-like transport to semiconducting properties typical of heavily doped semiconductors. The proximity to a semiconducting state results in a substantial enhancement of the thermoelectric performance typified by a maximum ZT of 0.65 at 800 K for x close to the highest nominal content (x = 3.8 - 3.9).[10,11] The main ingredient leading to this high ZT value is the very low lattice thermal conductivity (κ_L ~ 0.5 - 0.7 $W.m^{-1}.K^{-1}$) observed in the $Ag_xMo_9Se_{11}$ compounds. This encouraging result clearly shows that further investigating the thermoelectric properties of this class of materials containing high nuclearity Mo clusters may be a worthwhile way of research to pursue.

While studying the $Ag_xMo_9Se_{11}$ family of compounds, we tried to substitute a fraction of Ag by In to enhance the atomic mass fluctuations throughout the crystal lattice (i.e. the disorder). This substitution might introduce an additional source of phonon scattering thereby enabling to achieve lower thermal conductivity values and thus, larger *ZT* values. However, this attempt failed and led to a multiphase sample. Based on a single-crystal X-ray diffraction study, the majority phase of this sample was identified to be the new quaternary compound $Ag_3In_2Mo_{15}Se_{19}$. Here, we present a detailed investigation of the synthesis, the crystal and electronic structures as well as the low- and high-temperature thermoelectric properties of this new Mo-cluster material. Further characterization of this compound was carried out through low-temperature Hall effect experiments (5 – 300 K) and specific heat measurements in a wide temperature range (2 – 1200 K).

EXPERIMENTAL SECTION

Synthesis. Starting materials used for the solid-state syntheses were $MoSe_2$, InSe, Ag (Strem, 3N5), and Mo, all in powder form. Before use, Mo powder (Plansee 4N) was reduced under H_2 flowing gas at 1000°C during ten hours in order to eliminate any trace of oxygen. The molybdenum diselenide was prepared by the reaction of selenium (Umicore 5N) with H_2 reduced Mo in a ratio 2:1 in an evacuated (ca. 10^{-2} Pa Ar residual pressure) and flame-baked silica tube, heated at about 700°C during two days. InSe was synthesized from the elements (In shots Strem Chemicals 3N) heated at 800°C in evacuated silica tube. All starting reagents were found monophasic on the basis of their powder X-ray diffraction diagram made on a D8 Bruker Advance diffractometer equipped with a LynxEye detector ($CuK\alpha_1$ radiation). Furthermore, in order to avoid any contamination by oxygen and moisture, the starting reagents were kept and handled in a purified argon-filled glovebox. $Ag_3In_2Mo_{15}Se_{19}$ was first observed as single-crystals in an attempt to insert indium in $Ag_{3.5}Mo_9Se_{11}$. The stoichiometry was only known after a complete structural study on one of these single crystals by X-ray diffraction. Subsequently, we could get a single-phase powder sample, as shows it the X-ray diagram on Figure 1, by heating the

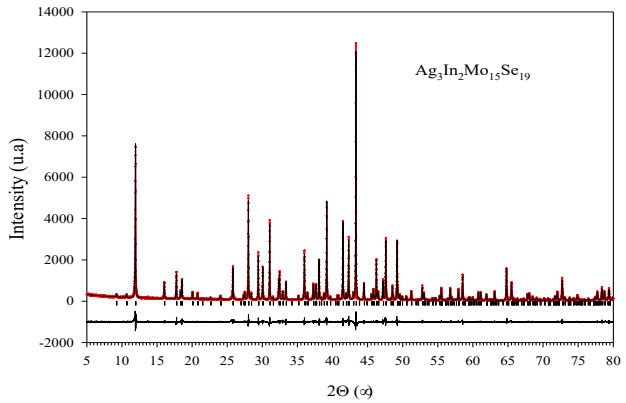

Figure 1. Observed (red crosses), calculated (black line) and difference profiles for the refinement of $Ag_3In_2Mo_{15}Se_{19}$ in profile-matching mode (λ = 1.5406 Å).

required stoichiometric mixture of Ag, Mo, InSe, and $MoSe_2$ in a sealed molybdenum crucible at 1300 °C during 40 hours. The analysis of X-ray diagrams of powders heated at 1300°C for 40 hours with starting compositions $Ag_xIn_2Mo_{15}Se_{19}$ with x ranging between 2 and 3 showed that a single phase was only observed for x comprised between 2.9 and 3. Beyond these limits, multi-phase samples with $In_2Mo_{15}Se_{19}$, $MoSe_2$ and $(Ag,In)Mo_6Se_8$ as main impurities were obtained

Hot Uniaxial Pressing (HUP). The obtained samples of $Ag_3In_2Mo_{15}Se_{19}$ were ground and subsequently densified by HUP sintering that was carried out under vacuum (about 10^{-2} mbar). The pressing conditions were the following: the pressure was applied from the beginning of the temperature increase (8 °C/min) to the end of the high temperature dwell. Typical quantity of 5 g of $Ag_3In_2Mo_{15}Se_{19}$ powders were introduced into the Ø 12 mm graphite dies previously coated with boron nitride. The applied load was 50 MPa at the beginning of the heating and was gradually increased to 85 MPa when the sintering temperature, 1300 °C, was reached. The dwell time was 2 h for all experiments. The densities for all pellets were calculated to be around 98% of the theoretical values after measuring volume and weight.

Single crystal structure determination. A black crystal of dimensions 0.237 x 0.162 x 0.111 mm^3 was selected for data collection. Intensity data were collected on a Nonius Kappa CCD diffractometer using a graphite-monochromatized MoK_α radiation (λ = 0.71073Å) at room temperature. The COLLECT program package[12] was used to establish the angular scan conditions (φ and ω scans) during the data collection. The data set was processed using EvalCCD[13] for the integration procedure. An absorption correction (Tmin = 0.1848, Tmax 0.0243) was applied using the description of the crystal faces.[14] The structure was solved by direct methods using Sir97[15] and subsequent difference Fourier syntheses in the space group R-3c. All structure refinements and Fourier syntheses were carried out using JANA2006.[16] At this stage, difference-Fourier map revealed significant electron densities near the atoms In (3.35/-3.00 e $Å^{-3}$), and Ag (3.52/-2.35 e $Å^{-3}$). Third-order tensors in the Gram-Charlier expansion[17] of the indium and silver displacement factors were used to better describe the electronic density around these cationic sites. The residual R value dropped to 0.0293 and the residual peaks in the vicinity of In to 0.53 and -0.84 e $Å^{-3}$, and Ag to 1.74 and -0.73 e $Å^{-3}$. The non-harmonic probability density function maps of In, and Ag did not show significant negative region indicated that the refined model can be considered as valid.[18] The Figure 2 shows the isosurfaces of the probability density for the Ag and In atoms.

(a) (b)

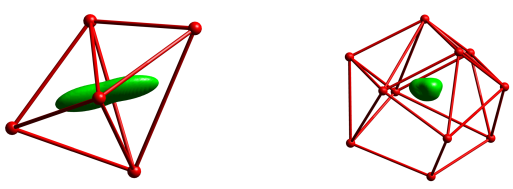

Figure 2. Non-harmonic probability density isosurface of (a) Ag, and (b) In. Se atoms are drawn at an arbitrary size. Level of the three-dimensional maps are at 0.05 $Å^{-3}$.

Refinement of the occupancy factor of Ag atom led to the final stoichiometry $Ag_{2.99}In_2Mo_{15}Se_{19}$. Crystallographic data and X-ray

structural analysis for the $Ag_3In_2Mo_{15}Se_{19}$ compound are summarized in Table 1, and selected interatomic distances are listed in Table 2.

Table 1: Crystal and structure refinement data for $Ag_3In_2Mo_{15}Se_{19}$.

Formula	$Ag_3In_2Mo_{15}Se_{19}$
Formula weight	3492.6
Crystal system	trigonal
Space group	R-3c
a (Å)	9.9755(1)
c (Å)	57.2943(9)
Volume (Å^3)	4937.5(1)
Z	6
ρ_{calc} (g/cm^3)	7.0452
Radiation, wavelength (Å)	MoKα, 0.71073 Å
Temperature of measurement (K)	293
2Θmax (deg)	43.97
Reflections collected/unique/Rint	47059/4280/0.0706
Reflections with I>2σ(I)	3048
Crystal dimensions (mm^3)	0.237 x 0.162 x 0.111
Absorption coefficient (mm^{-1})	29.852
Absorption correction	Semi-empirical from equivalents
Max./min. transmission	0.1848/0.0243
Goodness-of-fit on F^2	1.08
R indices [I > 2σ(I)], R1, wR2	0.0293, 0.0512
R indices (all data), R1, wR2	0.0555, 0.0562
Largest diff. peak and hole (e Å^{-3})	1.95, -1.76

Table 2. Selected Interatomic Distances for $Ag_3In_2Mo_{15}Se_{19}$.

Mo1-Mo1	2.6784(3)	In-Se5	2.9893(12)
Mo1-Mo1	2.7007(2)	In-Se2	3.2806(2)
Mo1-Mo2	3.5694(4)	In-Se2	3.2806(4)
Mo1-Se4	2.5812(4)	In-Se2	3.2806(3)
Mo1-Se2	2.6340(4)	In-Se1	3.5812(6)
Mo1-Se1	2.5726(3)	In-Se1	3.5812(6)
Mo1-Se1	2.5854(3)	In-Se1	3.5812(6)
Mo1-Se1	2.6173(4)		
Mo2-Mo2	2.6455(2)	Ag-Se2	2.677(3)
Mo2-Mo3	2.7763(2)	Ag-Se2	2.726(3)
Mo2-Mo3	2.6820(2)	Ag-Se3	2.5885(9)
Mo2-Se5	2.5339(4)	Ag-Se4	2.881(2)
Mo2-Se2	2.5675(4)		
Mo2-Se2	2.6538(5)		
Mo2-Se1	2.6947(3)		
Mo2-Se3	2.6699(2)		
Mo3-Mo3	2.7334(4)		
Mo3-Se2	2.6265(3)		
Mo3-Se2	2.6264(4)		
Mo3-Se3	2.5729(3)		
Mo3-Se3	2.5729(3)		

Computational procedure. Self-consistent ab initio band structure calculations were performed on the model compound $Ag_3In_2Mo_{15}Se_{19}$ with the scalar relativistic tight-binding linear muffin-tin orbital (LMTO) method in the atomic spheres approximation including the combined correction.[19] Exchange and correlation were treated in the local density approximation using the von Barth - Hedin local exchange correlation potential.[20] Within the LMTO formalism interatomic spaces are filled with interstitial spheres. The optimal positions and radii of these additional "empty spheres" (ES) were determined by the procedure described in ref. 21. Eight non-symmetry-related ES with 1.48 Å ≤ r_{ES} ≤ 2.49 Å were introduced for the calculations on $Ag_3In_2Mo_{15}Se_{19}$. The full LMTO basis set consisted of 5s, 5p, 4d and 4f functions for Mo and Ag spheres, 5s, 5p, 5d, 4f for In spheres, 4s, 4p, and 4d for Se spheres, and s, p, and d functions for ES. The eigenvalue problem was solved using the following minimal basis set obtained from the Löwdin downfolding technique: Mo 5s, 5p, 4d ; Ag 5s, 5p, 4d; In 5s, 5p; Se 4s, 4p; and interstitial 1s LMTOs. The k space integration was performed using the tetrahedron method.[22] Charge self-consistency and the average properties were obtained from 417 irreducible k points for $Ag_3In_2Mo_{15}Se_{19}$. A measure of the magnitude of the bonding was obtained by computing the crystal orbital Hamiltonian populations (COHP) which are the Hamiltonian population weighted density of states (DOS).[23] As recommended,[24] a reduced basis set (in which all ES LMTO's have been downfolded) was used for the COHP calculations. Bands, DOS and COHP curves are shifted so that ε_F lies at 0 eV.

Transport properties measurement. The densified ingots were cut with a diamond wire saw into bar-shaped (~ 2×2×8 mm^3) and cylinder-shaped samples (10 mm in diameter and 2 mm thick) to determine their physical properties. The measurement of the thermoelectric properties at low temperature (2 – 300 K) was carried out using the thermal transport option (TTO) of the physical properties measurement system (PPMS, Quantum Design). The TTO allows sequential measurements of the electrical resistivity, Seebeck voltage and thermal conductivity at each selected temperature. The contacts were realized by attaching four copper leads onto the sample using conducting silver epoxy. A temperature gradient was established by heating one end of the specimen while maintaining the other end to a low-temperature reservoir. Calibrated cernox thermometers were attached to the sample 5 mm apart. The temperature difference and the voltage were monitored at the same positions along the sample. Hall coefficient measurements were conducted between 5 and 300 K on the same sample using a five-probe method with the AC transport option of the PPMS using copper wires attached with a tiny amount of silver paste. The transverse electrical resistivity ρ_{xy} was measured while sweeping the magnetic field from −5 to +5T. To dismiss any magnetoresistive contribution due to misalignments of the contacts, the Hall voltage ρ_H was derived from the antisymmetric part of ρ_{xy} under magnetic field reversal following the formula $\rho_H = \left[\rho_{xy}(+\mu_0 H) - \rho_{xy}(-\mu_0 H)\right]/2$.

For measurements over the temperature range of 300 – 1000 K, the thermopower and the electrical resistivity were simultaneously measured with a ZEM3 system (ULVAC-RIKO) under partial helium atmosphere on the bar-shaped sample. The thermal conductivity κ was determined in the same temperature range via thermal diffusivity (LFA 427, NETZSCH) measurements on the prism-shaped sample. Both properties are related by the formula $\kappa = aC_P\rho_V$ where a is the thermal diffusivity, C_P is the specific heat and ρ_V is the thermal expansion coefficient. Specific heat measurements (DSC 403 F3, NETZSCH) were carried out under argon atmosphere while the thermal expansion of the unit cell was not taken into account in the present study.

Uncertainties in the electrical resistivity, Hall coefficient, thermopower and thermal conductivity measurements are estimated to 5%, 5%, 5% and 8 %, respectively. An overall good match between the low-temperature and high-temperature data sets was observed, the deviation being at most 10 %.

RESULTS AND DISCUSSION

Crystal Structure. A view of the crystal structure of $Ag_3In_2Mo_{15}Se_{19}$ is shown in Figure 3. The Mo-Se framework is

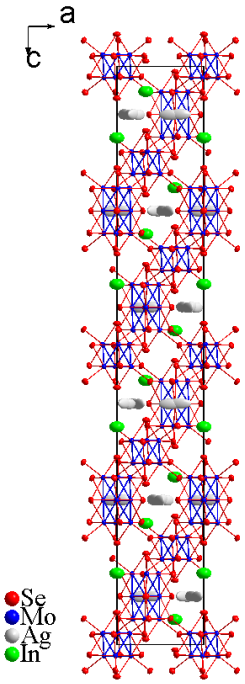

Figure 3. View of the crystal structure of $Ag_3In_2Mo_{15}Se_{19}$ along the b axis. Ellipsoids are drawn at the 97 % probability level.

similar to that of $In_2Mo_{15}Se_{19}$[25] and is based on an equal mixture of $Mo_6Se_8^iSe_6^a$ and $Mo_9Se_{11}^iSe_6^a$ cluster units interconnected through Mo-Se bonds (for details of the i- and a-type ligand notation, see Ref. 26) (Fig. 4). The first unit can be described as a Mo_6 octahedron surrounded by 8 face-capping inner Se^i (6 Se1 and 2 Se4) and 6 apical Se^a (Se2) ligands. The Mo_9 core of the second unit results from the face sharing of 2 octahedral Mo_6 clusters. The Mo_9 cluster is surrounded by 11 Se^i atoms capping the faces of the bioctahedron and 6 apical Se^a ligands above the ending Mo atoms. The $Mo_6Se_8^iSe_6^a$ and $Mo_9Se_{11}^iSe_6^a$ units are centered at 6b and 6a positions and have the point-group symmetry -3 and 32, respectively. The Mo-Mo distances within the Mo_6 clusters are 2.6784 (3) Å for the intra-triangle distances (distances within the Mo_3 triangles formed by the Mo1 atoms related through the three-fold axis) and 2.7007 (2) Å for the inter-triangle distances. In $In_2Mo_{15}Se_{19}$, the two later values are larger, 2.686 (2) and 2.772(10) Å, respectively. This reflects the different cationic charge transfers towards the Mo_6 clusters in the two parent compounds. Indeed, the contraction of the Mo_6 cluster observed in the Ag-filled compound corresponds to an augmentation of the number of electrons on the Mo_6 cluster as previously observed in the MMo_6X_8 series when the cationic charge increases.[5] The Mo-Mo distances within the Mo_9 clusters are 2.6455 (2) and 2.7334 (4) Å for the distances in the triangles formed by the Mo2 and Mo3 atoms, respectively. In $In_2Mo_{15}Se_{19}$, the corresponding distances are equal to 2.674 (2) and 2.680 (4) Å. The distances between the triangles formed by the Mo2 and Mo3 atoms are 2.6820 (2) and 2.7763 (2) Å in $Ag_3In_2Mo_{15}Se_{19}$ compared to 2.712(5) and 2.808(6) Å in $In_2Mo_{15}Se_{19}$. Although, the structural response of the Mo_9 cluster with respect to the increase of the charge transfer is more complex, we observe that the Mo2-Mo2 intratriangle as well as the two Mo2-Mo3 intertriangle distances are shorter in the Ag-filled compound. On the other hand, a slight increase of the Mo3-Mo3 bonds occurs in the median Mo_3 triangle (2.680 (4) Å in $In_2Mo_{15}Se_{19}$). Nevertheless, the overall effect is again a contraction of the cluster as reflected by the interplane distance Δ(2)-Δ(3) which decreases from 2.280 to 2.263 Å. This trend is analogous to that reported for the series $In_xMo_{15}Se_{19}$ ($2.9 \le x \le 3.4$) when the indium content x increases.[27] The latter compounds also contain Mo_6Se_8 and Mo_9Se_{11} units but arranged in a different way. The Mo-Se distances are nearly unaffected by the cationic charge and range between 2.5726 (3) and 2.6340

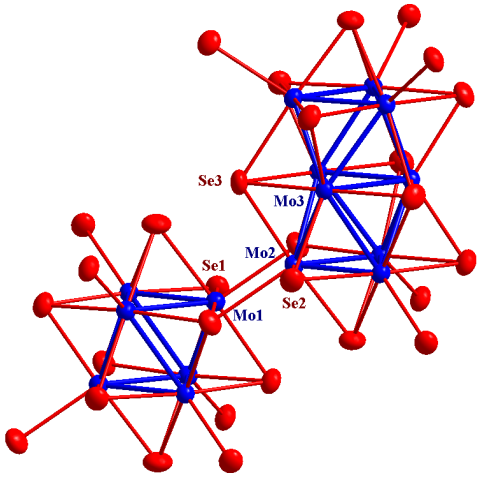

Figure 4. Plot showing the atom-numbering scheme and the inter-unit linkage of the $Mo_6Se_8Se_6$ and $Mo_9Se_{11}Se_6$ units.

(4) Å within the $Mo_6Se_8^iSe_6^a$ unit and between 2.5339 (4) and 2.6947 (3) Å within the unit, as usual. Finally, the three-dimensional packing arises from the interconnection of the $Mo_6Se_8^iSe_6^a$ and $Mo_9Se_{11}^iSe_6^a$ cluster units through Mo-Se bonds. Indeed, each $Mo_6Se_8^iSe_6^a$ unit is interconnected to 6 $Mo_9Se_{11}^iSe_6^a$ units (and vice-versa) via Mo1-Se2 bonds (respectively Mo2-Se1) to form the three-dimensional Mo-Se framework, the connective formula of which is $[Mo_6Se_2^iSe_{6/2}^{i-a}]Se_{6/2}^{a-i}$ $[Mo_{11}Se_5^iSe_{6/2}^{i-a}]Se_{6/2}^{a-i}$. It results from this arrangement that the shortest intercluster Mo1-Mo2 distance between the Mo_6 and Mo_9 clusters is 3.5694 (4) Å compared to 3.389(3) Å in $In_2Mo_{15}Se_{19}$, indicating only weak metal-metal interaction.

The Ag atoms occupy distorted triangular bipyramid sites located between two consecutive In sites with Ag-Se distances ranging from 2.5885 (9) to 2.881 (2) Å (Figure 5). This insertion leads to a modification of the In environment due to its displacement towards the Se5 atoms and to the receding of the Se3 atoms. Indeed, in $In_2Mo_{15}Se_{19}$, each In atom is in pentacapped trigonal prismatic environment of selenium atoms with In-Se distances ranging from 3.162 (2) to 3.800(4) Å, while in $Ag_3In_2Mo_{15}Se_{19}$, the In cation has seven Se atoms as nearest neighbors with In-Se distances in the ranges 2.9893 (12) - 3.5812 (6) Å. These seven Se atoms form a monocapped octahedron compressed along the three-fold axis. The three Se3 atoms at 3.800 (4) Å from the In atom in $In_2Mo_{15}Se_{19}$ are now at 4.19 Å in $Ag_3In_2Mo_{15}Se_{19}$.

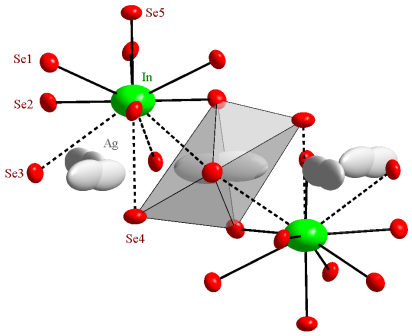

Figure 5. Selenium environments for the In and Ag atoms (ellipsoids at the 97 % probability level).

Electronic structure. Several theoretical studies have been devoted to Mo_6 and Mo_9 cluster based chalcogenides.[9,28] In most cases, the band structure of these compounds can be explained on the basis of the electronic structure of the cluster units: Inter-cluster interactions that may occur hardly modify the main features of the molecular orbital (MO) pattern of the cluster in the three-dimensional solid. The MO diagram of Mo_6Se_8 shows a significant HOMO/LUMO gap that separates Mo-Mo bonding and non-bonding MOs from antibonding MOs for the metallic electron (ME) count, electrons that are available for metal-metal bonding, of 24.[28a] The extended Hückel MO diagram of the Mo_9Se_{11} unit shows an overall non-bonding MO lying in the middle of a large gap, so that the favored ME count of this motif is equal to 36 or 38 depending upon the occupation of this MO.[28a] A more recent study based on DFT calculations showed that the corresponding MO is slightly Mo-Mo antibonding and rather high in energy so that the optimal ME count of the Mo_9Se_{11} cluster is equal to 36 ME.[28b] Therefore assuming an ionic interaction between the cations and the molybdenum selenide network as well as an insignificant interaction between Mo_6 and Mo_9 clusters in a first approach, the band structure of such compound should exhibit a gap that divides Mo—Mo bonding bands from Mo-Mo antibonding bonds. DOS and Mo-Mo COHP curves of $In_2Mo_{15}Se_{19}$ computed within a DFT approach are sketched in Figure 6 and 7. Since bands that lie in the vicinity of the Fermi level are mainly centered on molybdenum, only Mo-projected DOS are drawn. The density of states at the Fermi level is centered on metallic atoms of both Mo_6 and Mo_9 clusters. A band gap of a width equal to 0.25 eV appears ca. 0.40 eV above the Fermi level. As shown by the COHP curves, this gap lies between low—lying Mo—Mo bonding and non-bonding bands and high—lying metal—metal antibonding bands. In $In_2Mo_{15}Se_{19}$, the total ME count is equal to 54 because of the monovalent character of indium. Since the optimal ME counts of Mo_6 and Mo_9 clusters are equal to 24 and 36, respectively, 6 extra electrons are needed to reach the optimal ME count of both clusters. These extra electrons can be supplied by insertion of cations such as alkaline, alkaline earth, or transition metals. Assuming a rigid band model and an ionic interaction of the inserted atoms in $In_2Mo_{15}Se_{19}$, the additional electrons will be located in the bands that lie just above the Fermi level and Mo-Mo bond distances should change in accordance with their COHP. In the case of $Ag_3In_2Mo_{15}Se_{19}$, variations of Mo—Mo bond lengths fully agree with the expected one on the basis of the COHP computed for $In_2Mo_{15}Se_{19}$. A major part of Mo—Mo bonds of $Ag_3In_2Mo_{15}Se_{19}$ are shortened compared to the parent compound since bands that lie just above the Fermi level in $In_2Mo_{15}Se_{19}$ show a significant Mo—Mo bonding character (see Fig. 7 b—d, f). Conversely, the Mo3—Mo3 bond is lengthened since the bands above the Fermi level in $In_2Mo_{15}Se_{19}$ exhibit an antibonding character for this contact (see Fig. 7 a). Finally, the very weak shortening of the intra-triangle Mo1-Mo1 bond is consistent with the non-bonding character of the bands of the lowest empty bands of the band structure of $In_2Mo_{15}Se_{19}$. These results reinforce our approaches that consider an electronic donation of the inserted metal atom towards the molybdenum selenide clusters.

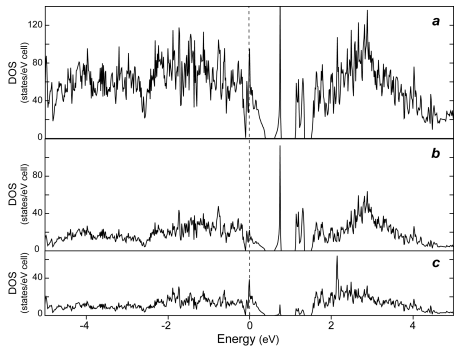

Figure 6. DOS curves for $In_2Mo_{15}Se_{19}$: (a) total, (b) Mo_9–projected, (c) Mo_6–projected.

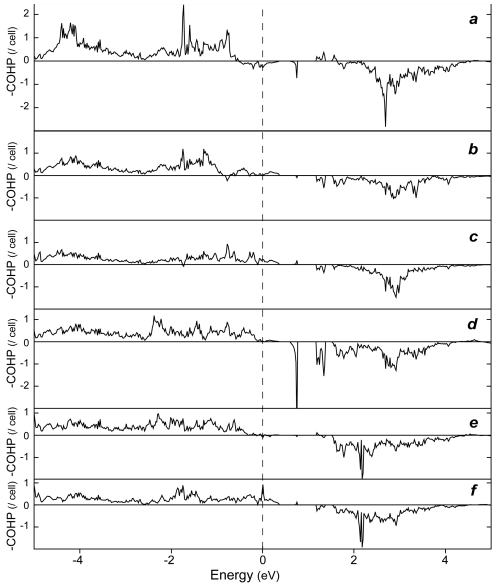

Figure 7. COHP curves for Mo-Mo bonds: (a) 2.680 Å, (b) 2.712 Å, (c) 2.808 Å, (d) 2.674 Å, (e) 2.686 Å, (f) 2.772 Å computed for $In_2Mo_{15}Se_{19}$. (a–d) and (e–f) curves correspond to Mo-Mo bonds of Mo_9 and Mo_6 motifs, respectively.

The DOS curves computed for the model compound $Ag_3In_2Mo_{15}Se_{19}$ are sketched in Figure 8. Assuming the donation of one electron per inserted silver atoms, as it is confirmed by the computed atomic charge, the total ME count per formulation unit reaches 54 + 3 = 57. This ME count is lower that the one corresponding to a semiconducting state, *i. e.* 60 ME. The DOS thus suggests a *p*-type metallic behavior. It is worth pointing that a pseudo gap lies a few hundredth of eV below the Fermi level. Considering the following formula $Ag_{3-x}In_2Mo_{15}Se_{19}$ corresponding to a lack of a few silver atoms, the title compound may behave as a semimetal.

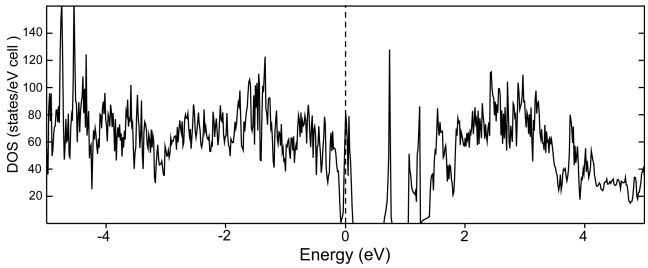

Figure 8. LMTO DOS of $Ag_3In_2Mo_{15}Se_{19}$.

Electronic Properties. Figure 9 shows the temperature dependence of the electrical resistivity. Two distinct features can be identified in the $\rho(T)$ data: a sharp drop in the ρ values at $T \sim 7$ K and a switch in the electrical conduction from a semiconducting-like behaviour below 100 K to a metallic-like one above this temperature. This last behaviour remains unaffected upon further increasing T up to 800 K. The sudden decrease in $\rho(T)$ near 7 K may suggest that a magnetic or a structural phase transition set in. However, as we shall see below, no fingerprints of such transitions could be detected in other transport data suggesting either an electronic origin or the presence of a small fraction of secondary phase which becomes superconducting at ~ 7 K. The latter possibility may be related to Chevrel phases $M_xMo_6Se_8$ that can show superconductivity depending on the nature of the M atoms.[6] In the present case, both $InMo_6Se_8$ and $AgMo_6Se_8$ undergo a superconducting transition at 8.2 and 5.9 K, respectively, and may therefore explain the observed drop in $\rho(T)$.[29,30] The second turn over occurring near 100 K may result from a balance between the variations in the carrier concentration and in their mobility. However, as we shall see below, this scenario is not applicable here since both holes and electrons participate to the transport suggesting that the temperature dependence of the concentrations and mobilities of each carrier give rise to the observed behaviour of $\rho(T)$.

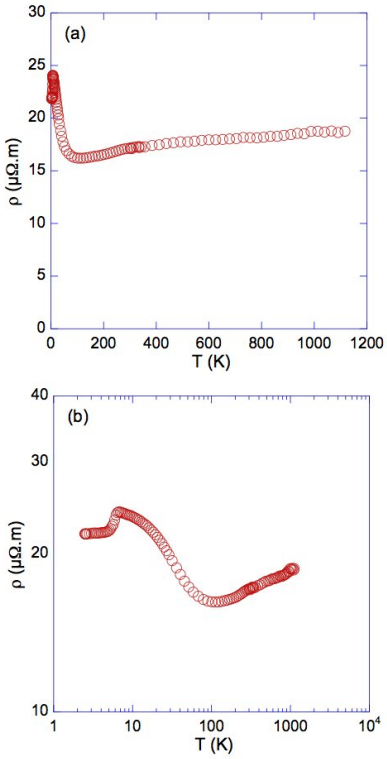

Figure 9. (a) Electrical resistivity versus temperature. (b) Log-log plot of the low-temperature data to underline the sharp drop that sets in at ~ 7 K.

Figure 10 depicts the Hall resistivity ρ_H as a function of the

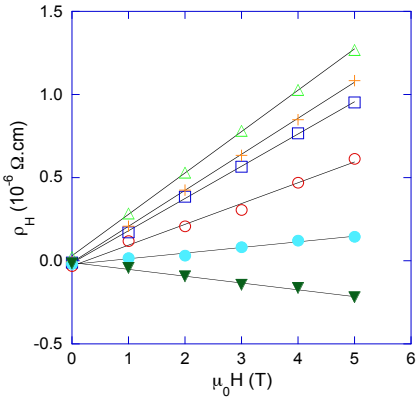

Figure 10. Hall resistivity ρ_H as a function of the applied magnetic field $\mu_0 H$ measured at (▼) 15, (●) 25, (+) 55, (Δ) 100, (□) 200 and (o) 300 K. The solid lines represent the best linear fit to the data.

applied magnetic field $\mu_0 H$ at selected temperatures. Above 10 K, all the $\rho_H(\mu_0 H)$ curves exhibit a linear field dependence in the field range covered. The positive slope corresponds to an electrical conduction dominated by holes. Below 25 K, however, the positive slope turns into a negative one revealing the presence of electrons that dominates the low-temperature magnetotransport. The temperature dependence of the Hall coefficient R_H, extracted from the slope of the isothermal $\rho_H(\mu_0 H)$ curves, is depicted in Figure 11. Up to 100 K, the

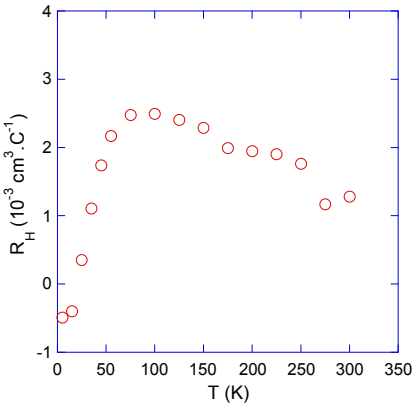

Figure 11. Temperature dependence of the Hall coefficient R_H.

R_H values increase while above this temperature, the variations are strongly lessened though still discernable. Together with the switch from a hole-like to an electron-like signal below 25 K, this temperature dependence suggests a multiband character of the electrical conduction in this material. In such a case, the carrier concentration derived from the R_H values using the single-carrier relations $n = -1/R_H e$ and $p = 1/R_H e$ (e is the elementary charge) for electrons and holes, respectively, stands for upper limits of the actual electron and hole concentrations. A more detailed quantitative analysis would then require to apply a two-band model to derive the temperature dependence of n and p. This modelling is beyond the scope of the present study and we therefore restrict our analysis to a derivation of the carrier concentrations within a single-band picture. The hole concentration remains nearly constant in the 50 – 300 K temperature range and amounts to 3×10^{21} cm^{-3}. As for the Hall mobility, defined as $\mu_H = R_H/\rho$, a single-band model gives a lower limit of the hole and electron mobilities. In the present case, μ_H is of the order of a few cm^2.V^{-1}.s^{-1} above 50 K (Figure 12). These low values are coherent

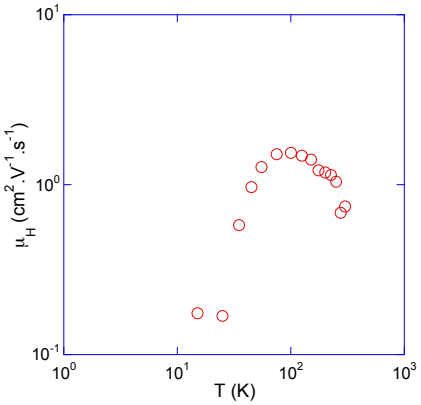

Figure 12. Hall mobility as a function of temperature in log-log format.

with the presence of Mo *d*-states near the Fermi level usually leading to low μ_H values as already observed in Chevrel phases and in $Ag_xMo_9Se_{11}$.[7,11]

Further information on the scattering mechanisms of the charge carriers can be obtained from the $\mu_H(T)$ data. In the conventional theory of itinerant charge carriers, $\mu_H(T)$ can be modelled by a simple power law T^{-s} when one scattering mechanism limits the mobility for the temperature range of interest. The value of the exponent s reflects the dominant source of diffusion of the charge carriers and can be equal to $-3/2$, 0 or $3/2$ for acoustic phonon, neutral impurities and ionized impurities scattering, respectively. Figure 12 suggests that ionized impurities may dominate the transport between 20 and 100 K while above this temperature, a decrease in μ_H with T is observed. A fit of the mobility data between 100 and 300 K using a power law leads to an exponent of ~ - 0.75. This value may point to the presence of multiple scattering mechanisms and might be a sign of the influence of acoustic phonon scattering becoming increasingly important as T rises. Alternatively, other scattering mechanisms may play a role in the temperature dependence observed. Besides the three conventional mechanisms mentioned above, optical phonons could also limit the mobility of the carriers giving rise to a $T^{-1/2}$ dependence. Though usually observed at high temperatures, this mechanism

cannot be ruled out in the present case. Further Hall effect measurements above 300 K would be helpful in determining the exact nature of the scattering mechanisms in this material.

The temperature dependence of the thermopower is depicted in Figure 13. Across the entire temperature range investigated, α

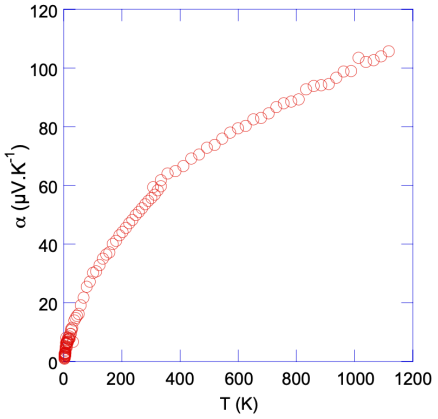

Figure 13. Temperature dependence of the Seebeck coefficient.

is positive indicative of holes as the dominant charge carrier. α increases with increasing temperature to reach ~ 80 $\mu V.K^{-1}$ at 800 K. The non-linear behaviour in the $\alpha(T)$ data contrasts with a linear dependence expected in a metallic state for which thermal diffusion of the charge carriers prevails. In the present case, $\alpha(T)$ shows a temperature dependence that mimics that of heavily doped semiconductors for which the non-linearity arises due to a loss of degeneracy when the Fermi level nears the valence or conduction band edges. However, in light of the above-mentioned Hall data, the temperature dependence may originate from a balance between the hole and electron contribution to the thermopower.

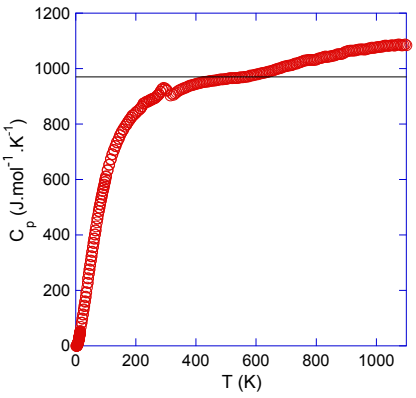

Figure 14. Specific heat C_P versus temperature. The solid line represents the Dulong-Petit estimation.

Thermal Properties. Figure 14 shows the temperature dependence of the specific heat C_P from 2 up to 1200 K. Neither structural nor superconducting transition could be evidenced suggesting that the anomaly observed in the $\rho(T)$ data is not intrinsic to this compound. The low-temperature $C_P(T)$ data enables to get information on the density of states at the Fermi level and to extract the Debye temperature. Using the conventional Fermi-liquid relation $C_P/T = \gamma + \beta T^2$, where γ is the electronic contribution and βT^2 is the phononic contribution, a fit in the 4 – 15 K^2 range yields 54.8 $mJ.mol^{-1}.K^{-2}$ and 0.0189 $mJ.mol^{-1}.K^{-4}$ for γ and β, respectively. The former is related to $N(E_F)$ via $\gamma = 0.176N(E_F)$ where γ and $N(E_F)$ are expressed in $mJ.mol^{-1}.K^{-2}$ and $states.Ry^{-1}.(f.u.)^{-1}$, respectively. The γ value leads to an experimental $N(E_F)$ value of 23 $states.eV^{-1}.(f.u.)^{-1}$, in fair agreement with our band structure calculations (37.5 $states.eV^{-1}.(f.u.)^{-1}$). The difference between the experimental and theoretical values may be related to the sensitivity of $N(E_F)$ to the exact position of the Fermi level, located in the present case in a strongly-varying DOS region. The coefficient β can be utilized to derive the Debye temperature θ_D from $\theta_D = \left(\frac{12\pi^4 NR}{5\beta}\right)^{\frac{1}{3}}$ where N is the number of atoms per formula unit and R is the gas constant. This formula results in a very low value of 159 K. As we shall see below, this value correlates with the low thermal conductivity exhibited by this compound.

At high temperatures, the Dulong-Petit law is usually employed to estimate $C_P(T)$. This law provides a constant value, which stands for the contribution of the lattice vibrations of a harmonic crystal. In real crystals, however, $C_P(T)$ can largely exceed this value since the anharmonicity of the lattice vibrations, primarily arising from the thermal expansion of the unit cell, is not taken into account. The difference between this approximation and the measured data can be easily observed in Figure 14. The Dulong-Petit law is valid near 300 K and up to 600 K while above the latter this approximation breaks down. In the whole temperature range, the $C_P(T)$ data increase linearly following the linear function $C_P(T) = 0.28454T + 837.54\ J.mol^{-1}.K^{-1}$.

This fit was used to calculate the temperature dependence of the total thermal conductivity shown in Figure 15a.

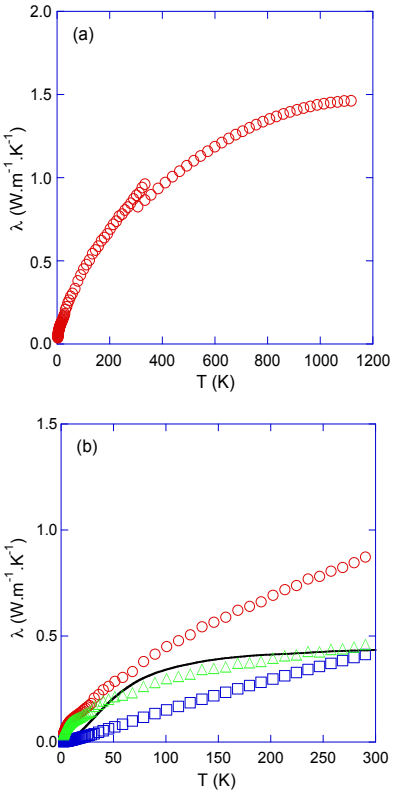

Figure 15. Temperature dependence of the (a) total thermal conductivity and (b) lattice thermal conductivity. The estimated values are close to the theoretical calculated using Eq.(3).

κ increases monotonically with temperature to reach 1.4 W.m^{-1}.K^{-1} at 800 K. This behaviour is at odd with that of a dielectric crystal for which a dielectric maximum at very low temperatures followed by a T^{-1} dependence is expected. The observed behaviour is reminiscent to glassy systems and several crystallographic features may explain this dependence in the present case. The complex crystalline structure exhibiting a high degree of disorder is likely the main ingredient that strongly shortens the phonon mean free path. The large anisotropic thermal motion of the Ag atoms might constitute an additional mechanism leading to a strong dampening of the acoustic heat-carrying waves. Even though our X-ray diffraction studies have provided evidence for abnormally large thermal displacement parameters, further spectroscopic tools such as inelastic neutron scattering would be helpful in determining whether the dynamical motion of these atoms plays a significant role.

The separation of the lattice and the electronic contributions to the thermal conductivity can be achieved via an estimation of the latter component by the Wiedemann-Franz law $\kappa_e = LT/\rho$ where L is the Lorenz number. A simple assumption consists of taking the value of a degenerate electron gas i.e. $L = L_0 = 2.44\times10^{-8}\ V^2.K^{-2}$. Even though this approximation is reasonable at low temperatures (T < 300 K), it usually fails to describe the electronic contribution of the thermal conduction at higher temperatures in heavily-doped semiconductors or in materials with low κ values and a non-negligible κ_e contribution. The $Ag_3In_2Mo_{15}Se_{19}$ compound stands for a prominent example of the latter since using $L = L_0$ would result in unphysical κ_L values near 1100 K and even to negative values above this temperature. Hence, above 300 K, the temperature dependence of L has to be taken into account to obtain a more accurate assessment of the lattice contribution. As a first approximation, we tried to estimate L using a single-parabolic-band model. Within this description, the Lorenz number is expressed as

$$L = \frac{k_B^2}{e^2}\frac{(1+\lambda)(3+\lambda)F_\lambda(\eta)F_{2+\lambda}(\eta) - (2+\lambda)^2F_{1+\lambda}(\eta)^2}{(1+\lambda)^2F_\lambda(\eta)^2} \quad (1)$$

where k_B is the Boltzmann constant, e is the elementary charge, λ is a scattering constant related to the energy dependence of the electronic scattering mechanism and F_i is the Fermi integral of order i defined as $F_i(\eta) = \int_0^\infty \frac{\xi^i d\xi}{1+\exp[\xi-\eta]}$ where ξ is the reduced energy of charge carriers and η is the reduced Fermi level defined as $\eta = E_F/k_BT$. In Eq.(1), we utilized the η values inferred from the analysis of the thermopower data using

$$\alpha = -\frac{k_B}{e}\left(\frac{(2+\lambda)F_{1+\lambda}(\eta)}{(1+\lambda)F_\lambda(\eta)} - \eta\right) \quad (2)$$

The Hall data have shown that, near 300 K, either neutral impurity and acoustic phonon or optical phonon scattering may be held responsible for the $\mu_H(T)$ data. These scattering mechanisms result in $\lambda = 1/2$, $\lambda = 0$ and $\lambda = 1$, respectively. In addition, we assumed that a single mechanism dominates the hole diffusion. This model then leads to L values of 2.32×10^{-8}, 2.18×10^{-8} and $2.39\times10^{-8}\ V^2.K^{-2}$, respectively. These different values result in very similar lattice contribution κ_L which amounts to ~ 0.5 W.m^{-1}.K^{-1} at 300 K (Figure 15b). This extremely low value, similar to those of other Mo-cluster compounds,[7,10,11] indicates that efficient phonon-scattering mechanisms limit the heat transport in this compound.

It is instructive to compare the lattice contribution to the minimum thermal conductivity (also referred as the amorphous limit) calculated following the model developed by Cahill, Watson and Pohl and based on the Einstein's model of the thermal conductivity of crystalline solids.[32,33] In this model, the minimum thermal conductivity κ_{min} is given by[32]

$$\kappa_{min} = \left(\frac{\pi}{6}\right)^{\frac{1}{3}} k_B V^{-\frac{2}{3}} \sum_i v_i \left(\frac{T}{\theta_i}\right)^2 \int_0^{\theta_i/T} \frac{x^3 e^x}{(e^x-1)^2}\,dx \quad (3)$$

where the summation is performed over one longitudinal and two transverse modes. In this formula, V is the average volume per atom, $\theta_i = v_i(\hbar/k_B)(6\pi^2/V)^{1/3}$, and v_i are the Debye temperature, and the sound velocity associated to the longitudinal and transverse modes, respectively. In the present case, the values of the transverse and longitudinal velocities of sound, v_T and v_L respectively, were measured at room temperature on an isostructural compound ($Ag_3Tl_2Mo_{15}Se_{19}$) and equal to 1680 and 3350 $m.s^{-1}$, respectively. As shown in Figure 15b, the κ_L values approach the amorphous limit at 300 K

indicating that the phonon mean free path is close to the mean value of the interatomic distances. Above 300 K, it seems therefore reasonable to assume that $\kappa_L(T)$ is practically temperature-independent and very close to the amorphous limit of ~ 0.38 $W.m^{-1}.K^{-1}$.

Combining the electrical resistivity, the thermopower and the total thermal conductivity, the temperature dependence of ZT can be calculated and is illustrated in Figure 16. The maximum value of 0.45 achieved at 1100 K is lower than those obtained in the $Cu/FeMo_6Se_8$ and $Ag_xMo_9Se_{11}$ (x = 3.8) compounds (ZT = 0.6 at 1150 K and 0.65 at 800 K, respectively).[7,10,11] This difference can be attributed to the multiband nature of the electrical conduction preventing to achieve high thermopower values in $Ag_3In_2Mo_{15}Se_{19}$.

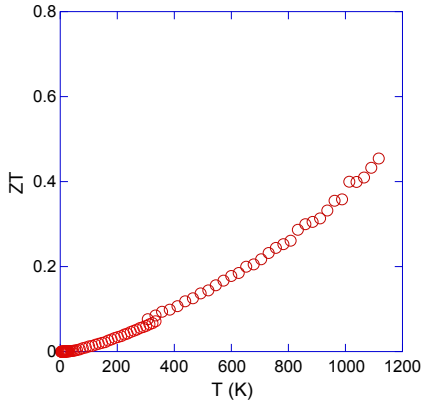

Figure 16. Temperature dependence of the thermoelectric figure of merit ZT.

CONCLUSION

In summary, we have presented the crystal structure of the new quaternary Mo-cluster compound $Ag_3In_2Mo_{15}Se_{19}$. Single crystal X-ray diffraction study shows that the crystal structure is built by the Mo_6Se_8 and Mo_9Se_{11} cluster units found in the crystal structure of the Chevrel phase and of the $Ag_xMo_9Se_{11}$ compounds, respectively. Electronic band structure calculations revealed that the Fermi level lies within the valence bands in agreement with the hole-dominated transport properties. The complex crystal structure combined with large anisotropic thermal displacement parameters of the Ag atoms stands for two essential features governing the thermal transport in this compound. The low thermal conductivity values, comparable to those observed in the Chevrel and the $Ag_xMo_9Se_{11}$ phases, are the key ingredient leading to a relatively high ZT of 0.45 at 1100K. Further optimization of the thermoelectric properties may be achieved by suppressing the multiband conduction to enhance the thermopower values. This may be realized via substituting Ag/In by other cations and/or by introducing other elements on the Mo/Se sites.

ASSOCIATED CONTENT

Supporting Information. Crystallographic data in CIF format. This information is available free of charge via the Internet at http://pubs.acs.org.

AUTHOR INFORMATION

Corresponding Author

*E-mail: patrick.gougeon@univ-rennes1.fr; bertrand.lenoir@ijl.nancy-universite.fr.

REFERENCES

(1) Picard, S.; Halet, J.-F.; Gougeon, P.; Potel, M. *Inorg. Chem.* **1999**, *38*, 4422-4429 and references therein.

(2) Slack, G. A. CRC Handbook of Thermoelectrics (Ed.: D. M.Rowe), CRC, Boca Raton, FL, 1995, p. 407.

(3) Goldsmid, H. J. in *Thermoelectric Refrigeration* (Temple Press Books Ltd, London, 1964).

(4) Chevrel, R.; Sergent, M.; Prigent, J. *J. Solid State Chem.* **1971**, *3*, 515.

(5) Yvon, K. in *Current Topics in Material Science* (Ed. Kaldis), North-Holland Amsterdam, 1979, vol. 3, p. 53.

(6) Fischer, Ø. *Appl. Phys.* **1978**, *16*, 1.

(7) Caillat, T.; Fleurial, J.-P.; Snyder, G.J. *Solid State Sci.* **1999**, *1*, 535-544.

(8) (a) Gougeon, P.; Potel, M.; Padiou, J.; Sergent, M. Comptes Rendus De L Academie Des Sciences Serie Ii 1983, 296, 351-354. (b) Gougeon, P.; Padiou, J.; Lemarouille, J. Y.; Potel, M.; Sergent, M., *J. Solid State Chem.* **1984,** *51*, 218-226.

(9) Gougeon, P.; Potel, M.; Gautier, R. *Inorg. Chem.* **2004,** *43*, 1257-1263.

(10) Zhou, T.; Lenoir, B.; Candolfi, C.; Dauscher, A.; Al Orabi, R.; P. Gougeon, P.; Potel, M.; Guilmeau, E. *J. Elec. Mat.* **2011**, 40, 508-512.

(11) Zhou, T.; Lenoir, B.; Colin, M.; Dauscher, A.; Gall, P.; P. Gougeon, P.; Potel, M.; Guilmeau, E. *Appl. Phys. Lett.* **2011**, *98*, 162106.

(12) Nonius BV (1999). COLLECT, data collection software, Nonius BV

(13) Duisenberg, A. J. M. PhD thesis, University of Utrecht (NL), 1998.

(14) de Meulenaer, J. ; H. Tompa, H., *Acta Crystallogr., Sect. A: Found. Crystallogr.* **1965**, *19*, 1014-1018.

(15) Altomare, A.; Burla, M. C.; Camalli, M.; Cascarano, G. L.; Giacovazzo, C.; Guagliardi, A.; Moliterni, A. G. G.; Polidori, G.; Spagna, R. *J. Appl. Crystallogr.* **1999**, *32*, 115.

(16) Petricek, V.; Dusek, M. Jana2000, Institute of Physics, Academy of Sciences of the Czech Republic: Prague, Czech Republic, 2000.

(17) Johnson, C. K.; Levy, H. A. (1974). International Tables for X-ray Crystallography, Ed. J. A. Ibers & W. C. Hamilton, Vol. IV, pp. 311-336. Birmingham: Kynoch Press.

(18) Bachmann, R.; Schulz, H. *Acta Cryst.* **1984**, *A40*, 668-675.

(19) a) Andersen, O. K. *Phys. Rev. B* **1975**, *12*, 3060; b) Andersen, O. K. *Europhysics News* **1981**, *12*, 4; c) Andersen, O. K. in *The Electronic Structure Of Complex Systems*, Eds. P. Phariseau, and W. M. Temmerman, Plenum Publishing Corporation, New York, 1984; d) Andersen, O. K.; Jepsen, O. *Phys. Rev. Lett.* **1984**, *53*, 2571. e) Andersen, O. K.; Jepsen, O.; Sob, M. in *Electronic Band Structure and its Application*, Ed. M. Yussouf, Springer-Verlag, Berlin, 1986; f) Skriver, H. L. The LMTO Method, Springer-Verlag, Berlin, 1984.

(20) von Barth, U.; Hedin, L. *J. Phys. C.* **1972**, *5*, 1629.

(21) Jepsen, O.; Andersen, O. K. *Z. Phys. B* **1995**, *97*, 35.

(22) Blöchl, P. E.; Jepsen, O.; Andersen, O. K. *Phys. Rev. B* **1994**, *49*, 16223.

(23) Dronskowski, R.; Blöchl, P. E. *J. Phys. Chem.* **1993**, *97*, 8617.

(24) Jepsen, O.; Andersen, O. K.; personal communication.

(25) Potel, M.; Chevrel, R.; Sergent, M., *Acta Crystallogr. Sect. B-Structural Science* **1981**, *37*, 1007-1010.

(26) Schäfer, H.; Von Schnering, H. G. *Angew. Chem.* **1964**, *20*, 833.

(27) Gruttner, A.; Yvon, K.; Chevrel, R.; Potel, M.; Sergent, M.; Seeber, B. *Acta Cryst.* **1979**, *B35*, 285.

(28) (a) Hughbanks, T.; Hoffmann, R. *J. Am. Chem. Soc.* **1983**, *105*, 1150. (b) Gautier, R.; Gougeon, P.; Halet, J.-F.; Potel, M.; Saillard, J.-Y. *J. Alloys Compd.* **1997**, *262-263*, 311-315. (c) Gautier, R.; Picard, S.; Gougeon, P.; Potel, M. *Mat. Res. Bull.* **1999**, *34*, 1, 93-101. (d) Picard, S.; Halet, J.-F.; Gougeon, P.; Potel, M. *Inorg. Chem.* **1999**, *38*, 4422-4429. (e) Picard, S.; Saillard, J.-Y.; Gougeon, P.; Noël, H.; Potel, M. *J. Solid State Chem.* **2000**, *155*, 417. (f) Salloum, D.; Gautier, R.; Gougeon, P.; Potel, M. *J. Solid State Chem.* **2004**, *177*, 1672-1680. (g) Salloum, D.; Gougeon, P.; Potel, M.; Gautier, R. *C.R. Chim.* **2005**, *11-12*, 1743-1749. (h) Gougeon, P.; Salloum, D.; Cuny, J.; Le Pollès, L.; Le Floch, M.; Gautier, R.; Potel, M. *Inorg. Chem.* **2009**, *48*, 8337-8341. (i) Gougeon, P.; Gall, P.; Gautier, R.; Potel, M. *Acta Crystallogr., Sect. C: Cryst. Struct. Commun.* **2010**, C66, i67-i70

(29) Sergent, M.; Chevrel, R. *J. Solid State Chem.* **1973**, *6*, 433.

(30) Tarascon, J. M.; Disalvo, F. J.; Murphy, D. W.; Hull, G.; Waszczak, J. V. *Phys. Rev. B* **1984**, *29*, 172-180.

(31) Fistul, V. I. in Heavily Doped Semiconductors (Plenum Press, New York, 1969).

(32) Cahill, D. G.; Watson, S. K.; Pohl, R. O. *Phys. Rev. B* **1992**, *46*, 6131.

(33) Einstein, A. *Ann. Phys.* **1911**, *35*, 679.

SYNOPSIS TOC. $Ag_3In_2Mo_{15}Se_{19}$ constitutes an Ag-filled variant of $In_2Mo_{15}Se_{19}$ containing Mo_6 and Mo_9 clusters. Its metallic behavior is in agreement with electronic band structure calculations carried out using the LMTO method. The complex unit cell together with the cage-like structure of $Ag_3In_2Mo_{15}Se_{19}$ results in very low thermal conductivity values leading to a ZT of 0.45 at 1100 K.